

Astronomy & Astrophysics manuscript no.  
(will be inserted by hand later)

# Radiation Transfer of Emission Lines in Curved Space-Time

Steven V. Fuerst and Kinwah Wu

Mullard Space Science Laboratory, University College London, Holmbury St Mary, Surrey RH5 6NT, UK  
e-mail: [svf@mssl.ucl.ac.uk](mailto:svf@mssl.ucl.ac.uk), [kw@mssl.ucl.ac.uk](mailto:kw@mssl.ucl.ac.uk)

Received:

**Abstract.** We present a general formulation for ray-tracing calculations in curved space-time. The formulation takes full account of relativistic effects in the photon transport and the relative motions of the emitters and the light-of-sight absorbing material. We apply the formulation to calculate the emission from accretion disks and tori around rotating black holes. In our model the emission lines and continuum originate from an accretion disk or torus, and the motion of the emitters in the disk/torus is determined by the gravity of the black hole and the space-time structure near the black hole. The line-of-sight absorbing medium is comprised of cold absorbing cloudlets. These cloudlets are kinematically hot, with their velocity dispersion determined by the local virial temperature. The emission from the accretion disk/torus is resonantly absorbed/scattered. Our calculations demonstrate that line-of-sight absorption significantly modifies the profiles of lines from the accretion disks. It is often difficult to disentangle absorption effects from other geometrical and kinematics effects, such as the viewing inclination and the spin of the black hole. Our calculations also show that emission lines from accretion tori and from thin accretion disks differ substantially. Large geometrical obscuration could occur in tori, and as a consequence lines from tori generally have much weaker redshift wings at large viewing inclination angles. Moreover, the blue peak is truncated.

**Key words.** accretion, accretion disks — black hole physics — galaxies: active — line: profiles — radiative transfer — relativity

## 1. Introduction

The strong X-rays observed in active galactic nuclei (AGN) and some X-ray binaries are believed to be powered by accretion of material into black holes. The curved space-time around the black hole influences not only the accretion hydrodynamics but also the transport of radiation from the accretion flow.

Emission lines from thin Keplerian disks around non-relativistic stellar objects generally have two symmetric peaks (Smak 1969), corresponding to the approaching and receding line-of-sight velocities due to disk rotation. Because of various relativistic effects, lines from accretion disks around black holes do not always have symmetrical double-peak profiles. The accretion flow near a black hole is often close to the speed of light, and emission is relativistically boosted. The blue peak of the line therefore becomes stronger and sharper. Moreover, the strong gravity near the black-hole event horizon causes time dilation, which shifts the line to lower energies. Emission lines from accretion disks around black holes appear to be broad, with a very extended red wing and a narrow, sharp blue peak (see e.g. the review by Fabian et al. (2000) and references therein). Furthermore, gravitational lensing

can produce multiple images and self-occultation, further modifying the emission line profile.

Various methods have been used to calculate the profiles of emission lines from accretion disks around black holes. The methods can be roughly divided into three categories. We now discuss each of them briefly. The first method uses a transfer function to map the image of the accretion disk onto a sky plane (Cunningham 1975, 1976). The accretion disk is assumed to reside in the equatorial plane. It is Keplerian and geometrically thin, but optically thick. The space-time metric around the black hole is first specified, and the energy shift of the emission (photons) from each point on the disk surface is then calculated. A parametric emissivity law for the disk emission is usually used — typically, a simple power-law which decreases radially outward. The specific intensity at each point in the sky plane is determined from the energy shift and the corresponding specific intensity at the disk surface, using the Lorentz-invariant property. The transfer-function formulation (Cunningham 1975, 1976) has been applied to line calculations in settings ranging from thin accretion rings (e.g. Gerbal & Pelat 1981) and accretion disks around Schwarzschild (e.g. Laor 1991) and rotating (Kerr) black holes (e.g. Bromley, Chen & Miller 1997). The second method makes use of the impact parameter of photon

orbits around Schwarzschild black holes (e.g. Fabian et al. 1989; Stella 1990; Kojima 1991). The transfer function in this method is described in terms of elliptical functions, which are derived semi-analytically. The Jacobian of the transformation from the accretion disk to sky plane is, however, determined numerically via infinitesimal variations of the impact parameter (Bao 1992). The method can be generalized to the case of rotating black holes by using additional constants of motion (Viergutz 1993; Bao, Hadra & Ostgaard 1994; Fanton et al. 1997; Cadez, Fanton & Calvani 1998). The third method simply considers direct integration of the geodesics to determine the photon trajectories and energy shifts (Dabrowski et al. 1997; Pariev & Bromley 1998; Reynolds et al. 1999).

These calculations have shown how the dynamics of the accretion flow around the black hole and the curved space-time shape the line profiles. Various other aspects of the radiation processes, e.g. reverberation and reflection (Reynolds et al. 1999) and disk warping (Cadez et al. 2003) were also investigated using the methods described above. The results obtained from these calculations have provided us with a basic framework for interpreting X-ray spectroscopic observations, in particular, the peculiar broad Fe K $\alpha$  lines in the spectra of AGN, e.g. MCG-6-30-15 (Tanaka et al. 1995). While existing studies have put emphasis on the energy shift of the emission, transport effects such as extinction have been neglected. Resonant absorption (scattering) by ambient material can greatly modify the disk emission line profile. This effect was already demonstrated in a study by Ruszkowski & Fabian (2000), in which a simple rotating disk-corona provides the resonant scattering.

Here, we present ray-tracing calculations of spectra from relativistic flows in curved space-time. We include line-of-sight extinction and emission explicitly in the formulation. The radiative-transfer equation is derived from the Lorentz-invariant form of the conservation law. It reduces to the standard classical radiative-transfer equation in the non-relativistic limit. The formulation can incorporate dynamical and geometric models for the line-of-sight absorbing and emitting material. As an illustration, we calculate the emission line profiles from thin accretion disks and thick accretion tori around rotating black holes. The emitted spectra include a power law continuum together with a line. This emission is resonantly scattered by the line-of-sight material. We include the contribution from higher-order images and allow for self-occultation.

We organize the paper as follows. In §2 we show the derivation of the transfer equation. In §3 we construct the equation of motion for free particles in a Kerr space-time and for force-constrained particles for some simple parametric models. In §4 we construct a thin disk and a thick torus model. In §5 we generalize this by adding in absorption due to a distribution of absorbing clouds. In §6 we present the results from the models where either emission geometry (tori), or absorption (clouds) are important.

## 2. Radiative-Transfer Equation

Throughout this paper, we adopt the usual convention  $c = G = h = 1$  for the speed of light, gravitational constant and Planck constant. The interval in space-time is specified by

$$d\tau^2 = g_{\alpha\beta} dx^\alpha dx^\beta \quad (1)$$

where  $g_{\alpha\beta}$  is the metric.

Consider a bundle of particles which fill a phase-space volume element

$$d\mathcal{V} \equiv dx dy dz dp^x dp^y dp^z, \quad (2)$$

where  $dx dy dz (\equiv dV)$  is the three-volume and  $dp^x dp^y dp^z$  is the momentum range, at a given time  $t$ . Liouville's Theorem reads

$$\frac{d\mathcal{V}}{d\lambda} = 0 \quad (3)$$

(see Misner, Thorne & Wheeler 1973), with  $\lambda$  here being the affine parameter for the central ray in the bundle. The volume element  $d\mathcal{V}$  is thus Lorentz invariant.

The distribution function for the particles in the bundle,  $F(x^i, p^i)$  is given by

$$F(x^i, p^i) = \frac{dN}{d\mathcal{V}}, \quad (4)$$

where  $dN$  is the number of particles in the three-volume. Since  $dN/d\mathcal{V}$  is Lorentz invariant,  $F(x^i, p^i)$  is Lorentz invariant. From equation (2), we have

$$F = \frac{dN}{p^2 dV dp d\Omega}, \quad (5)$$

where  $p^2 dp d\Omega = dp^x dp^y dp^z$ . For massless particles,  $v = c = 1$  and  $|p| = E$ . The number of photons in the given spatial volume is therefore the number of photons flowing through an area  $dA$  in a time  $dt$ . It follows that

$$F = \frac{dN}{E^2 dA dt dE d\Omega}. \quad (6)$$

Recall that the specific intensity of the photons is

$$I_\nu = \frac{EdN}{dA dt dE d\Omega}, \quad (7)$$

By inspection of equations (6) and (7), we obtain

$$F = \frac{I_\nu}{E^3} = \frac{I_\nu}{\nu^3}, \quad (8)$$

where  $\nu (= E)$  is the frequency of the photon. We will use this Lorentz invariant intensity,  $\mathcal{I} \equiv F$ , in the radiative transfer formulation.

In a linear medium, extinction is proportional to the intensity, and the emission is independent of the intensity of the incoming radiation. The radiative transfer equation is therefore

$$\frac{d\mathcal{I}}{ds} = -\chi\mathcal{I} + \eta \left( \frac{\nu_0}{\nu} \right)^3, \quad (9)$$

where  $\chi$  is the absorption coefficient,  $\eta$  is the emission coefficient and  $ds$  is the length element the ray traverses. The equation in this form is defined in the observer's frame, and the absorption and emission coefficients are related to their counterparts in the rest frame with respect to the medium via

$$\chi = \left( \frac{\nu_0}{\nu} \right) \chi_0 , \quad (10)$$

$$\eta = \left( \frac{\nu}{\nu_0} \right)^2 \eta_0 , \quad (11)$$

where the subscript "0" denotes quantities in the local rest frame.

The relative energy / frequency shift in a moving medium with respect to an observer at infinity is given by

$$\frac{E_0}{E} = \frac{\nu_0}{\nu} = \frac{p^\alpha u_\alpha|_\lambda}{p^\alpha u_\alpha|_\infty} , \quad (12)$$

where  $u^\alpha$  is the four-velocity of the medium as measured by an observer, and

$$\frac{ds}{d\lambda} = -p^\alpha u_\alpha|_\infty . \quad (13)$$

The radiative transfer equation (equation [9]) in the co-moving frame is therefore

$$\frac{d\mathcal{I}}{d\lambda} = -p^\alpha u_\alpha|_\lambda [-\chi_0(x^\beta, \nu)\mathcal{I} + \eta_0(x^\beta, \nu)] \quad (14)$$

(see Baschek et al. 1997).

The results in the co-moving frame can be used to determine the intensity and frequency in the other reference frames. The ray is specified by choosing  $x^\alpha(\lambda_0)$  and  $p^\alpha(\lambda_0)$ . From the geodesic equation, we have  $dp^\alpha/d\lambda + \Gamma_{\beta\gamma}^\alpha p^\beta p^\gamma = 0$ , where we have scaled  $\lambda$  by  $m$  for massive, and by 1 for massless particles. The total derivative of  $\mathcal{I}$  is therefore

$$\begin{aligned} \frac{d\mathcal{I}}{d\lambda} &= \frac{\partial\mathcal{I}}{\partial x^\alpha} \frac{dx^\alpha}{d\lambda} + \frac{\partial\mathcal{I}}{\partial p^\alpha} \frac{dp^\alpha}{d\lambda} , \\ &= p^\alpha \frac{\partial\mathcal{I}}{\partial x^\alpha} - \Gamma_{\beta\gamma}^\alpha p^\beta p^\gamma \frac{\partial\mathcal{I}}{\partial p^\alpha} . \end{aligned} \quad (15)$$

This, combined with equation (14), yields

$$\begin{aligned} -p^\alpha u_\alpha|_\lambda [-\chi_0(x^\beta, \nu)\mathcal{I} + \eta_0(x^\beta, \nu)] \\ = p^\alpha \frac{\partial\mathcal{I}}{\partial x^\alpha} - \Gamma_{\beta\gamma}^\alpha p^\beta p^\gamma \frac{\partial\mathcal{I}}{\partial p^\alpha} , \end{aligned} \quad (16)$$

which is the same as that derived by Lindquist (1966) from the Boltzmann Equation.

The metric and the initial conditions define the rays (the photon trajectories in 3D space), and the solution can be obtained by direct integration along the ray. For simplicity, we assume the refractive index  $n = 1$  throughout the medium. The solution to equation (14) is then

$$\mathcal{I}(\lambda) = \mathcal{I}(\lambda_0) \exp \left( \int_{\lambda_0}^{\lambda} \chi_0(\lambda', \nu_0) u_\alpha p^\alpha d\lambda' \right) \quad (17)$$

$$- \int_{\lambda_0}^{\lambda} \exp \left( \int_{\lambda'}^{\lambda} \chi_0(\lambda'', \nu_0) u_\alpha p^\alpha d\lambda'' \right) \eta_0(\lambda', \nu_0) u_\alpha p^\alpha d\lambda' .$$

In the non-relativistic limit,  $u_\alpha p^\alpha = 1$ , and the equation recovers the conventional form (see Rybicki & Lightman 1979).

### 3. Particle Trajectories

#### 3.1. Free particles

To determine the photon trajectories we need to specify the metric of the space-time. We consider the Boyer-Lindquist coordinates:

$$\begin{aligned} dt^2 &= \left( 1 - \frac{2Mr}{\Sigma} \right) dt^2 + \frac{4aMr \sin^2 \theta}{\Sigma} dt d\phi - \frac{\Sigma}{\Delta} dr^2 \\ &\quad - \Sigma d\theta^2 - \left( r^2 + a^2 + \frac{2a^2 Mr \sin^2 \theta}{\Sigma} \right) \sin^2 \theta d\phi^2 , \end{aligned} \quad (18)$$

where  $M$  is the black hole mass, with the three vector  $(r, \theta, \phi)$  corresponding to spherical polar coordinates, and defining  $\Sigma = r^2 + a^2 \cos^2 \theta$  and  $\Delta = r^2 - 2Mr + a^2$ . The dimensionless parameter  $a/M$  specifies the spin of the black hole, with  $a/M = 0$  corresponding to a Schwarzschild (non-rotating) black hole and  $a/M = 1$  to a maximally rotating Kerr black hole.

The motion of a free particle is described by the Lagrangian:

$$\begin{aligned} \mathcal{L} &= \frac{1}{2} \left[ - \left( 1 - \frac{2Mr}{\Sigma} \right) \dot{t}^2 - \frac{4aMr \sin^2 \theta}{\Sigma} \dot{t} \dot{\phi} + \frac{\Sigma}{\Delta} \dot{r}^2 \right. \\ &\quad \left. + \Sigma \dot{\theta}^2 + \left( r^2 + a^2 + \frac{2a^2 Mr \sin^2 \theta}{\Sigma} \right) \sin^2 \theta \dot{\phi}^2 \right] \end{aligned} \quad (19)$$

(here  $\dot{x}^\alpha = dx^\alpha/d\lambda$ ). The Lagrangian does not depend explicitly on the  $t$  and  $\phi$  coordinates. The momenta in the four coordinates are therefore

$$p_t = \partial\mathcal{L}/\partial\dot{t} = -E , \quad (20)$$

$$p_r = \partial\mathcal{L}/\partial\dot{r} = \frac{\Sigma}{\Delta} \dot{r} , \quad (21)$$

$$p_\theta = \partial\mathcal{L}/\partial\dot{\theta} = \Sigma \dot{\theta} , \quad (22)$$

$$p_\phi = \partial\mathcal{L}/\partial\dot{\phi} = L . \quad (23)$$

with  $E$  being the energy of the particle at infinity and  $L$  the angular momentum in the  $\phi$  direction. The corresponding equations of motion are

$$\dot{t} = E + \frac{2r(r^2 + a^2)E - 2aL}{\Sigma\Delta} , \quad (24)$$

$$\dot{r}^2 = \frac{\Delta}{\Sigma} (H + E\dot{t} - L\dot{\phi} - \Sigma\dot{\theta}^2) , \quad (25)$$

$$\dot{\theta}^2 = \frac{1}{\Sigma^2} (Q + (E^2 + H)a^2 \cos^2 \theta - L^2 \cot^2 \theta) , \quad (26)$$

$$\dot{\phi} = \frac{2arE + (\Sigma - 2r)L/\sin^2 \theta}{\Sigma\Delta} , \quad (27)$$

where  $Q$  is Carter's constant (Carter 1968), and  $H$  is the Hamiltonian, which equals 0 for photons and massless particles and equals  $-1$  for particles with a non-zero mass. (See Reynolds et al. (1999) for more details.) For simplicity, we have set the black-hole rest mass equal to unity

( $M = 1$ ) in the equations above. This is equivalent to normalizing the length to the gravitational radius of the black hole (i.e., set  $R_g \equiv GM/c^2 = 1$ ), and we will adopt this normalization hereafter.

There are square terms of  $\dot{r}$  and  $\dot{\theta}$  in two equations of motion. They could cause problems when determining the turning points at which  $\dot{r}$  and  $\dot{\theta}$  change sign in the numerical calculations. To overcome this, we consider the second derivatives of  $r$  and  $\theta$  instead. From the Euler-Lagrange equation, we obtain

$$\ddot{r} = \frac{\Delta}{\Sigma} \left\{ \frac{\Sigma - 2r^2}{\Sigma^2} \dot{t}^2 + \frac{(r-1)\Sigma - r\Delta}{\Delta^2} \dot{r}^2 + r\dot{\theta}^2 + \sin^2 \theta \left( r + \frac{\Sigma - 2r^2}{\Sigma^2} a^2 \sin^2 \theta \right) \dot{\phi}^2 - 2a \sin^2 \theta \frac{\Sigma - 2r^2}{\Sigma^2} \dot{t}\dot{\phi} + \frac{2a^2 \sin \theta \cos \theta}{\Delta} \dot{r}\dot{\theta} \right\} \quad (28)$$

$$\ddot{\theta} = \frac{1}{\Sigma} \left\{ \sin \theta \cos \theta \left[ \frac{2a^2 r}{\Sigma} \dot{t}^2 - \frac{4ar(r^2 + a^2)}{\Sigma} \dot{t}\dot{\phi} - \frac{a^2}{\Delta} \dot{r}^2 + a^2 \dot{\theta}^2 + \frac{\Delta + 2r(r^2 + a^2)^2}{\Sigma^2} \dot{\phi}^2 \right] - 2r\dot{r}\dot{\theta} \right\}. \quad (29)$$

In terms of the momenta and the Hamiltonian, the equations above can be expressed as

$$\dot{p}_r = \frac{1}{\Sigma \Delta} \left[ (r-1) ((r^2 + a^2)H - \kappa) + r\Delta H + 2r(r^2 + a^2)E^2 - 2aEL \right] - \frac{2p_r^2(r-1)}{\Sigma}, \quad (30)$$

$$\dot{p}_\theta = \frac{\sin \theta \cos \theta}{\Sigma} \left[ \frac{L^2}{\sin^4 \theta} - a^2(E^2 + H) \right], \quad (31)$$

where  $\kappa = Q + L^2 + a^2(E^2 + H)$ . Equations (21), (22), (24), (27), (30) and (31) are the equations of motion.

### 3.2. Motion in the presence of external forces

The equations of motion obtained in the previous section are applicable to free particles only. In a general situation external (non-gravitational) forces may be present and we need to specify the external force explicitly in deriving the equations of motion. However, in the setting of accretion disks around black holes we can often treat the effect of the external force implicitly which we will discuss in more detail in the following subsections.

#### 3.2.1. Rotational and Pressure Supported Model

Here we consider a simple model such that

$$\dot{t} > \dot{\phi} \gg \dot{r} \gg \dot{\theta}. \quad (32)$$

As  $\dot{r}$  and  $\dot{\theta}$  are small in comparison with other quantities, they can be neglected as a first approximation.

The equation of motion reads

$$\frac{d^2 x^\nu}{d\lambda^2} + \Gamma_{\alpha\beta}^\nu u^\alpha u^\beta = a^\nu, \quad (33)$$

where  $a^\nu$  is the four-acceleration due to an external force per unit mass. For axisymmetry (which is a sensible assumption for accretion onto rotating black holes),  $d/d\phi = 0$  and  $a^\phi = 0$ . The identity  $u^\alpha u_\alpha = 0$  together with  $\dot{r} = 0$  and  $\dot{\theta} = 0$  imply that  $a^t = 0$ . We may also set  $a^r = 0$  for simplicity. Because we have an extra equation from the identity  $u^\alpha u_\alpha = -1$ ,  $a^\theta$  can be determined self-consistently under the approximation  $\dot{\theta} = 0$ . This scenario thus corresponds to flows supported by rotation in the  $\hat{r}$  direction and by pressure in the  $\hat{\theta}$  direction.

Inserting the affine connection coefficients for the Kerr metric into the equation of motion yields quantities identical to zero on the left hand side of the equations for the  $\hat{t}$  and  $\hat{\phi}$  directions. This leaves only the non-trivial momentum equation in the radial direction:

$$0 = - \left( \frac{\Sigma - 2r^2}{\Sigma^2} \right) \dot{t}^2 + 2 \left( \frac{\Sigma - 2r^2}{\Sigma^2} \right) a \sin^2 \theta \dot{t}\dot{\phi} - \left( r + a^2 \sin^2 \theta \left( \frac{\Sigma - 2r^2}{\Sigma^2} \right) \right) \sin^2 \theta \dot{\phi}^2, \quad (34)$$

which further simplifies to

$$\frac{r\Sigma^2 \sin^2 \theta}{2r^2 - \Sigma} \dot{\phi}^2 = \left( \dot{t} - a \sin^2 \theta \dot{\phi} \right)^2. \quad (35)$$

Here we choose the positive solution

$$\dot{t} = \left( \frac{\sqrt{r\Sigma \sin \theta}}{\sqrt{2r^2 - \Sigma}} + a \sin^2 \theta \right) \dot{\phi}, \quad (36)$$

which corresponds to the same rotation as the black hole. This solution thus allows the flow to match the rotation of a prograde accretion disk.

From the metric we have

$$1 = \left( 1 - \frac{2r}{\Sigma} \right) \dot{t}^2 + \frac{4ar \sin^2 \theta}{\Sigma} \dot{t}\dot{\phi} - \left( r^2 + a^2 + \frac{2a^2 r \sin^2 \theta}{\Sigma} \right) \sin^2 \theta \dot{\phi}^2. \quad (37)$$

Combining equations (36) and (37) yields

$$\Sigma \sin^2 \theta \left( \frac{r(\Sigma - 2r)}{2r^2 - \Sigma} + \frac{2\sqrt{r}a \sin \theta}{\sqrt{2r^2 - \Sigma}} - 1 \right) \dot{\phi}^2 = 1. \quad (38)$$

It follows that the components of the four-velocity are

$$\begin{aligned} \dot{t} &= \frac{1}{\zeta} \left( \Sigma \sqrt{r} + a \sin \theta \sqrt{2r^2 - \Sigma} \right), \\ \dot{r} &= 0, \\ \dot{\theta} &= 0, \\ \dot{\phi} &= \frac{\sqrt{2r^2 - \Sigma}}{\zeta \sin \theta}, \end{aligned} \quad (39)$$

where

$$\zeta = \sqrt{\Sigma \left( \Sigma(r+1) - 4r^2 + 2a \sin \theta \sqrt{r(2r^2 - \Sigma)} \right)}. \quad (40)$$

The marginally stable orbit for particles is defined by the surface where

$$\frac{\partial E}{\partial r} = 0. \quad (41)$$

From equations (24), (27) and (39), we have

$$E = \frac{1}{\zeta} \left( (\Sigma - 2r)\sqrt{r} + a \sin \theta \sqrt{2r^2 - \Sigma} \right) . \quad (42)$$

After differentiation, we remove the non-zero factors in the expression and obtain the condition

$$\Delta \Sigma^2 - 4r(2r^2 - \Sigma) \left( \sqrt{2r^2 - \Sigma} - a \sin \theta \sqrt{r} \right)^2 = 0 . \quad (43)$$

Setting  $a = 0$  gives  $r = 6$ , which is often regarded as the limit for the inner boundary of an accretion disk around a Schwarzschild black hole. This value is the same as that derived by Bardeen, Press & Teukolsky (1972) using  $\partial^2 p_r^2 / \partial r^2 = 0$ .

Before we proceed further, we must note that the expressions for the velocity components in equations (39) hold only for regions “sufficiently” far from the black-hole event horizon. The approximation that we adopt in the model breaks down when the square root in the denominator approaches zero. This occurs at the light circularisation radius  $r_{\text{cir}}$ , which is given by  $\zeta = 0$ , or equivalently

$$\Sigma(r+1) - 4r^2 + 2a \sin \theta \sqrt{r(2r^2 - \Sigma)} \Big|_{r=r_{\text{cir}}} = 0 . \quad (44)$$

Moreover, the assumption of  $\dot{\theta} = 0$  is also invalid for radii smaller than the radius of the marginally stable orbit — the flow is neither rotational nor pressure supported and it follows a geodesic into the event horizon.

### 3.2.2. Isobaric Surfaces

In a stationary accretion flow, the acceleration must be balanced by some forces, e.g. the gradient of gas or radiation pressure. As the local acceleration  $a^\alpha$  can be calculated from the rotation law  $\omega(r, \theta)$  we can derive a set of isobaric surfaces when a rotation law is given. For a barotropic equation of state of the accreting matter the isobaric surfaces coincide with the isopicnic (constant-density) surfaces.

The accelerations in the  $\hat{r}$  and  $\hat{\theta}$  directions are

$$-\frac{\Sigma}{\Delta} a^r = \frac{\Sigma - 2r^2}{\Sigma^2} \left( \dot{t} - a \sin \theta \dot{\phi} \right)^2 + r \sin^2 \theta \dot{\phi}^2 , \quad (45)$$

$$-\Sigma a^\theta = \sin \theta \cos \theta \left[ \frac{2r}{\Sigma^2} \left( a \dot{t} - (r^2 + a^2) \dot{\phi} \right)^2 + \Delta \dot{\phi}^2 \right] . \quad (46)$$

The surface of constant acceleration is given by

$$a_\alpha \frac{dx_{\text{surf}}^\alpha}{d\lambda} = 0 \quad (47)$$

(here and hereafter  $dx_{\text{surf}}^\alpha / d\lambda \equiv dx^\alpha / d\lambda|_{x_{\text{surf}}}$ ). The stationary condition implies  $dt/d\lambda = 0$ , and axisymmetry implies  $d\phi/d\lambda = 0$ . Without losing generality, we can choose  $t = \phi = 0$  on the surface. Thus, equation (47) becomes

$$\begin{aligned} 0 &= \frac{\Sigma a^r}{\Delta} \frac{dr_{\text{surf}}}{d\lambda} + \Sigma a^\theta \frac{d\theta_{\text{surf}}}{d\lambda} , \\ &= \beta_1 \frac{dr_{\text{surf}}}{d\lambda} + \beta_2 \frac{d\theta_{\text{surf}}}{d\lambda} , \end{aligned} \quad (48)$$

where

$$\begin{aligned} \beta_1 &= \frac{\Sigma - 2r^2}{\Sigma^2} \left( \frac{1}{\omega} - a \sin \theta \right)^2 + r \sin^2 \theta , \\ \beta_2 &= \sin \theta \cos \theta \left[ \Delta + \frac{2r}{\Sigma^2} \left( \frac{a}{\omega} - (r^2 + a^2) \right)^2 \right] , \end{aligned} \quad (49)$$

and  $dr_{\text{surf}}/d\lambda$  and  $d\theta_{\text{surf}}/d\lambda$  determine the intersection of the isobaric surfaces and the  $(r, \theta)$  plane. By rescaling equation (48) with a factor of  $\sqrt{\Delta/\Sigma}$  and making use of the invariance

$$-\left( \frac{d\tau}{d\lambda} \right)^2 = \frac{\Sigma}{\Delta} \dot{r}^2 + \Sigma \dot{\theta}^2 , \quad (50)$$

we obtain

$$\begin{aligned} \frac{dr_{\text{surf}}}{d\lambda'} &= \frac{\beta_1}{\sqrt{\beta_2^2 + \Delta \beta_1^2}} , \\ \frac{d\theta_{\text{surf}}}{d\lambda'} &= \frac{-\beta_2}{\sqrt{\beta_2^2 + \Delta \beta_1^2}} . \end{aligned} \quad (51)$$

These two differential equations can be solved numerically and yield the isobaric surface as a parametric function of  $\lambda'$ .

## 4. Model Accretion Disks and Tori

We now demonstrate using the equations of motion above to construct the emitter models. The first is a geometrically thin accretion disk, in which the emitting particles are in Keplerian motion. The second is a torus, a 3-dimensional object with non-negligible thickness.

### 4.1. Accretion Disk

When space-time curvature is important, the Keplerian angular velocity of a test particle around a gravitating object is no longer  $\omega_k = r^{-3/2}$ , the expression in flat space-time. Instead, the Keplerian angular velocity in a plane containing the gravitating object can be obtained by setting  $\theta = \pi/2$  in equations (39) and (40). Hence, the components of the four-velocity of the particles in the disk are

$$\begin{aligned} \dot{t} &= \frac{r^2 + a\sqrt{r}}{r\sqrt{r^2 - 3r + 2a\sqrt{r}}} , \\ \dot{r} &= 0 , \\ \dot{\theta} &= 0 , \\ \dot{\phi} &= \frac{1}{\sqrt{r}\sqrt{r^2 - 3r + 2a\sqrt{r}}} , \end{aligned} \quad (52)$$

and the rotational velocity of a Keplerian accretion disk around a black hole is

$$\omega_k = \frac{1}{r^{3/2} + a} , \quad (53)$$

(Bardeen, Press & Teukolsky 1972).

The relative energy shift of the emission between the disk particle and an observer at a large distance is determined by equation (12), with  $u^\alpha$  as given in equation

(52). Keplerian disk images can be found in many existing works (e.g. Bromley, Miller & Pariev 1998), and we do not show disk images here. The general characteristics are that a disk image is asymmetric, with the separatrix for the energy shift of the emission no longer bisecting the disk image into two equal sectors, one for red shift and another for blue shift. The whole disk appears to be reddened, especially at the inner rim.

#### 4.2. Accretion Torus

To determine the geometry and structure of an accretion torus self-consistently is beyond the scope of this paper. Here, we consider a simple parametric model, with an angular velocity profile given by

$$\omega = \frac{1}{(r \sin \theta)^{3/2} + a} \left( \frac{r_k}{r \sin \theta} \right)^n. \quad (54)$$

The quantity  $r_k$  is the radius (on the equatorial plane) at which the material moves with a Keplerian velocity. The parameter  $n$  adjusts the force term, such as a pressure gradient, to keep the disk particles in their orbits, and it determines the thickness of the torus. In this study we just take  $n = 0.21$  without losing generality. If the torus is supported by radiation pressure, its inner edge is determined by the intersection of the isobaric surface with either one of two surfaces. These two surfaces provide the constraints, inside which the pressure-supported solution does not hold. The first is a surface defined by the orbits of marginal stability. For  $\omega(r, \theta)$ , it is given by

$$0 = 2a \sin^4 \theta \left[ \frac{r^2}{\Sigma} - \left( r^2 + a^2 + \frac{a^2 r \sin^2 \theta}{\Sigma} \right) \frac{\Sigma - 2r^2}{\Sigma^2} \right] \omega^3 + \sin^2 \theta \left[ \left( \frac{6r(r^2 + a^2)}{\Sigma} + 3\Delta - \Sigma \right) \frac{\Sigma - 2r^2}{\Sigma^2} + r \left( 1 - \frac{2r}{\Sigma} \right) \right] \omega^2 - \frac{6ar \sin^2 \theta}{\Sigma} \left( \frac{\Sigma - 2r^2}{\Sigma^2} \right) \omega + \Delta \sin^2 \theta \omega \frac{\partial \omega}{\partial r} - \left( 1 - \frac{2r}{\Sigma} \right) \frac{\Sigma - 2r^2}{\Sigma^2}. \quad (55)$$

The second is the limiting surface where the linear velocity approaches the speed of light. It is given by

$$0 = \Sigma - 2r + 4ar\omega \sin^2 \theta - ((r^2 + a^2)\Sigma + 2a^2r \sin^2 \theta) \omega^2 \sin^2 \theta. \quad (56)$$

Usually the former is larger than the latter. The outermost of these two surfaces determines the inner boundary and hence the critical surface of the torus.

Figure 1 shows the critical density surfaces of two tori. The first torus is around a Schwarzschild black hole and the second torus is around a maximally rotating black hole. The tori are constructed such that their specific angular momentum has a profile similar to those of the simulated accretion disks in Fig. 3. of Hawley & Balbus (2002).

In our model the boundary surface of the torus is determined by a single parameter,  $n$ , which specifies the index of the angular-velocity power law. Its value is selected

such that the angular-velocity profile matches the profiles obtained by the numerical simulations — here we consider that of Hawley & Balbus (2002). Model tori can be constructed using various different methods. An example is that in a study of dynamical stability of tori around a Schwarzschild black hole carried out by Kojima (1986), the model parametrizes the angular momentum instead of the angular velocity. We note that the aspect ratios of the torus surfaces obtained by Kojima (1986) and those shown in Fig. 1. are similar.

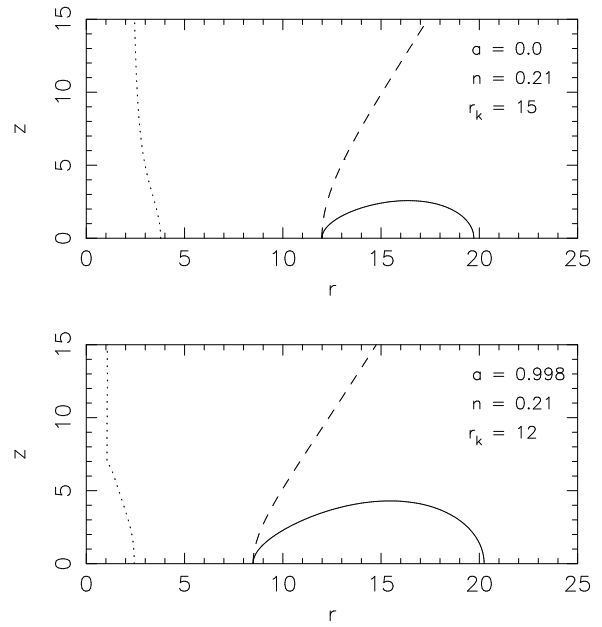


**Fig. 1.** The critical emitting surface of the torus (solid line), the surface defined by the orbits of marginal stability (dashed line) and the limiting surface where the linear velocity derived from equation (54) approaches the speed of light (dotted line) for a Schwarzschild black hole (top panel) and a Kerr black hole with  $a = 0.998$  (bottom panel). In both cases we consider an profile index  $n = 0.21$  (see Equation [54]), which gives the tori an angular momentum profile similar to those obtained in the accretion disk simulation of Hawley & Balbus (2002). The Kepler radius  $r_k$  is 15 for the Schwarzschild black hole and is 12 for the Kerr black hole.

#### 5. Extinction

The generic setting of the system under our investigation is that emitters with various strengths are distributed in space in a curved space-time, and the radiation is attenuated, and may be re-emitted, when propagating. The emitters and the line-of-sight material are in relativistic motion with respect to the observer and also with respect to each other. An example is that shown in Fig. 2., in which the emitters are the surface elements of an accretion disk and the absorbers are some clouds in the vicinity of the disk.

The photon trajectories and the motion of the emitters and absorbers are affected by the space-time distorted by the central black hole.

To construct the model we need to determine

- (i) the rays that connect the emitters, absorbers and observer,
- (ii) the four-velocities of the emitters and absorbers /scatterers,
- (iii) the spatial distributions of the emitters and the absorbers/scatterers, and
- (iv) the effective cross section of the absorbers/scatterers.

In the previous section, we have shown how to obtain (i) and (ii); in this section we incorporate (iii) and (iv) into the radiative-transfer calculations.

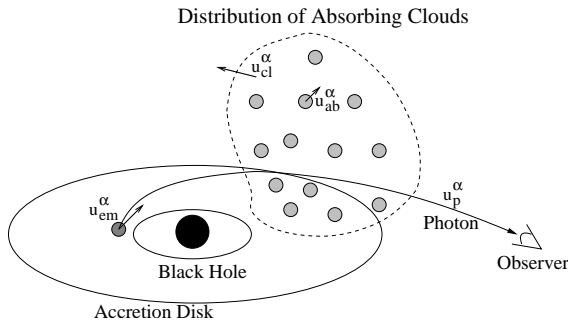


**Fig. 2.** A schematic illustration of the physical setting on which the radiative-transfer formulation is constructed. The space-time curvature is determined by a gravitating body, which is a rotating black hole. The emitting object is the accretion disk around the hole. The cloudlets in the vicinity attenuate the radiation from the accretion disk. The properties of the radiation are specified by the 4-velocity of the photon,  $u_p^\alpha$ . The other three important quantities in the model are the 4-velocity of emitting elements in the accretion disk  $u_{em}^\alpha$ , the bulk velocity of the absorbing cloudlets  $u_{cl}^\alpha$  and the “microscopic” 4-velocities of the cloudlets  $u_{ab}^\alpha$  with respect to the bulk motion of the cloudlets.

### 5.1. An illustrative model

We consider a model with the geometry shown in Fig. 2. The photons are emitted from the elements on the top and bottom surfaces of a geometrically thin disk in a Keplerian rotation around a Kerr black hole. The radiation is resonantly scattered (absorbed) by plasma clouds and is attenuated in its propagation. We omit emission from the clouds (i.e.  $\eta_0 = 0$  in equation [14]) in this study. The size of the clouds is small in comparison with the length scale of the system. They are not confined to be in the equatorial plane and are in orbital motion, supported by some implicit forces (which may be radiation, kinematic or magnetic pressure gradients). These clouds have a large

(thermal) distribution of velocities, in addition to their collective bulk velocity.

We assume that the radiation scattered into the energies of the lines is insignificant and ignore the photons that are scattered into the line-of-sight. Under this approximation, scattering simply removes the line photons and causes extinction similar to true absorption. Thus, for simplicity, hereafter we do not distinguish between scattering and absorption,<sup>1</sup> and the two terms are interchangeable, unless otherwise stated explicitly.

The rays originating from the accretion-disk surface that can reach the observer are determined by the 4-momenta of the photons, which are calculated using equations (24), (27) and (30). The 4-velocities of the emitting surface elements on the accretion disk are given by equations (52). These determine the relative energy shifts of the photons between the emitters and the observer. What we need next is to determine the relative energy shifts between the emitters and the absorbers. Then, we need a model mechanism by which the absorption takes place, and to derive the resonant absorption condition for the absorption coefficient.

Now we construct a model for the spatial distribution and the velocities of the absorbers. Consider a parametric model in which the bulk 4-velocities of the clouds are given by equations (39) and (40). In this model the bulk velocities of the clouds in the equatorial plane matches the 4-velocities of the accretion disk.

The clouds themselves are cold, and the thermal velocity of the gas particles inside are much smaller than their bulk motion and root-mean-square velocity dispersion. However, the clouds have a large velocity dispersion, given by the local virial temperature, which is comparable to the energy of the emission lines of interest. Therefore, the clouds can be considered as relativistic particles in the calculation. Using the bulk-motion velocities obtained by (39) and (40) together with the virial theorem, we can derive this temperature and determine the velocity distribution of the absorbing clouds.

The clouds fill most of space, with a radially dependent number density. However, close to the black hole, the assumptions above break down, and the axial force cannot support the clouds out of the equatorial plane. When this happens, they will flow along geodesics directly into the hole. In the numerical calculation, we determine the asymptotic boundaries at which the left hand sides of equations (44) and (43) vanish. This is done by evaluating these expressions and testing to see if they are negative at each point along the photon rays. Inside that surface, the number density of the clouds will be much less than that outside, which we approximate by setting it to zero in this zone.

<sup>1</sup> Here, in spite of the term “resonant scattering” (which describes the nature of the process), we have ignored the scattering of continuum photons into the line energy bins and the energy (frequency) redistribution in our calculations.

## 5.2. The absorption coefficient

We assume that the absorption is due to “cold” cloudlets with high virial velocities. The absorption coefficient of individual cloudlets is

$$\chi_i \propto \sigma \delta \left( \frac{u^\alpha k_\alpha + E_{\text{line}}}{E_\gamma} \right) \quad (57)$$

(with  $\sigma$  as the effective absorption cross section of the cloudlet, and  $k_\alpha$  the photon four-momentum). The absorption rest frequency is  $E_{\text{line}}$ , and  $E_\gamma$  is the energy of the photon in the bulk rest frame. The total effective absorption coefficient  $\chi_0$  is the sum of the contribution of these cloudlets, i.e.,

$$\chi_0 = \sum_i \chi_i . \quad (58)$$

Converting the sum into an integral in momentum space yields the absorption per unit length in the rest frame as

$$\chi_0 = \frac{-2\pi\lambda\sigma}{E_{\text{line}}^2} \times \iint p^2 dp d\mu \exp(-E/\Theta) u^\alpha k_\alpha \delta \left( \frac{u^\alpha k_\alpha + E_{\text{line}}}{E_\gamma} \right), \quad (59)$$

where we have defined  $\mu = \cos\theta$ ,  $\lambda$  is a normalization constant,  $\Theta$  is the temperature in relativistic units (with  $k_B = 1$ ), and  $E$  and  $p$  are the energy and momentum of a gas particle in the bulk rest frame. This form assumes isotropic thermal motion in the rest frame.

There are three terms that we need to determine before we can evaluate the integral, and they are the normalisation parameter  $\lambda$ , the temperature  $\Theta$  and the photon energy in the rest frame of the absorbing particle  $u^\alpha k_\alpha$ . When these variables are determined, we can then parametrise  $\sigma$  after integration is carried out.

### 5.2.1. The normalisation parameter $\lambda$

We now derive  $\lambda$  starting from

$$N = 4\pi\lambda \int_0^\infty p^2 dp \exp(-E/\Theta) , \quad (60)$$

where  $N$  is the number density of absorbing clouds. Integrating yields

$$\lambda = \frac{N \frac{m}{\Theta}}{4\pi m^3 K_2(\frac{m}{\Theta})} , \quad (61)$$

where  $K_\nu(x)$  is a modified Bessel function, and  $m$  is the average cloud mass. This is called the Jüttner distribution and corresponds to Maxwell's distribution except in the case of a relativistically high temperature.

### 5.2.2. The temperature $\Theta$

The total energy in the distribution of clouds is given by

$$E_{\text{tot}} = 4\pi\lambda \int_0^\infty p^2 dp E \exp(-E/\Theta) . \quad (62)$$

Integrating this yields the energy per unit mass as

$$\frac{E_{\text{tot}}}{Nm} = \frac{K_3(\frac{m}{\Theta})}{K_2(\frac{m}{\Theta})} - \frac{\Theta}{m} . \quad (63)$$

Using conservation of energy and angular momentum, we calculate the thermal energy of the virialised relativistic gas of absorbing clouds.

At infinity the medium has

$$E_{\text{init}} = Nm , \quad (64)$$

$$L_{\text{init}} = L_{\text{fin}} . \quad (65)$$

Close to the black hole it has

$$E_{\text{fin}} = \frac{Nm}{\zeta} \left[ (\Sigma - 2r)\sqrt{r} + a \sin \theta \sqrt{2r^2 - \Sigma} \right] , \quad (66)$$

$$L_{\text{fin}} = \frac{Nm}{\zeta} \left[ 2ar\sqrt{r} \sin^2 \theta - (r^2 + a^2) \sin \theta \sqrt{2r^2 - \Sigma} \right] \quad (67)$$

The energy released by the gas falling from infinity and slamming into a wall moving with a velocity given by equation (39) is

$$-E_{\text{tot}} = u^\alpha p_\alpha = -E_{\text{fin}} \dot{t}_{\text{init}} - L_{\text{fin}} \dot{\phi}_{\text{init}} . \quad (68)$$

After simplification, this becomes

$$- \frac{E_{\text{tot}}}{Nm} = \frac{1}{\zeta^2} \left[ (2r^2 - \Sigma)(r^2 + a^2) - 2ar \sin \theta \sqrt{r} \sqrt{2r^2 - \Sigma} - (a \sin \theta \sqrt{2r^2 - \Sigma} + \Sigma \sqrt{r}) \zeta \right] . \quad (69)$$

Thus the temperature of the media can be derived using equations (63) and (69). Unfortunately, this yields an implicit relation of  $m/\Theta$  that contains transcendental functions. The modified Bessel functions can be expanded in the limit where  $\Theta \ll m$  which corresponds to an “almost relativistic” gas. Since the potential energy released in accretion is of the order of a few percent of the rest mass of the infalling material, this approximation should hold in AGN.

Expanding to second order in  $\Theta/m$ , cancelling the exponential factors, and then solving the resulting quadratic yields

$$\frac{\Theta}{m} = \frac{2}{5} \left( -1 + \sqrt{1 + \frac{10}{3} \left( \frac{E_{\text{tot}}}{Nm} - 1 \right)} \right) . \quad (70)$$

Thus we have an explicit description of how the kinematic temperature varies with position.

### 5.2.3. The photon energy $u^\alpha k_\alpha$

In the rest frame, the motion of the thermalised medium is isotropic. Thus we can simplify the problem by aligning an axis along the photon propagation vector and working in a local Lorentz frame so that

$$k_\alpha = E_\gamma(-1, 1, 0, 0) , \quad (71)$$

and

$$p^\alpha = mu^\alpha = (E, p\mu, p_y, p_z) . \quad (72)$$

Thus,

$$u^\alpha k_\alpha = \frac{E_\gamma}{m} (p\mu - E) . \quad (73)$$

### 5.2.4. Evaluation of the $\delta$ -function

Using the relation that

$$\frac{d}{d\mu} \left[ \frac{u^\alpha k_\alpha + E_{\text{line}}}{E_\gamma} \right] = -\frac{p}{m}, \quad (74)$$

we obtain

$$\begin{aligned} \int d\mu u^\alpha k_\alpha \delta \left( \frac{u^\alpha k_\alpha + E_{\text{line}}}{E_\gamma} \right) \\ = \frac{u^\alpha k_\alpha}{\left| \frac{d}{d\mu} \left[ \frac{u^\alpha k_\alpha + E_{\text{line}}}{E_\gamma} \right] \right|} \Big|_{u^\alpha k_\alpha = -E_{\text{line}}} \\ = -E_{\text{line}} \frac{m}{p} \Big|_{u^\alpha k_\alpha = -E_{\text{line}}}. \end{aligned} \quad (75)$$

We change the variable  $pdp$  to  $EdE$ . The integral in equation (59) can now be simplified to

$$\chi_0 = \frac{2\pi\lambda\sigma m}{E_{\text{line}}} \int_{\frac{m}{2} \left( \frac{E_\gamma}{E_{\text{line}}} + \frac{E_{\text{line}}}{E_\gamma} \right)}^{\infty} EdE \exp(-E/\Theta) \quad (76)$$

Integrating this gives the absorption coefficient in the rest frame of the gas

$$\begin{aligned} \chi_0 = \frac{N\sigma}{2K_2(\frac{m}{\Theta})} \left[ \frac{1}{2} \left( \frac{E_\gamma}{E_{\text{line}}} + \frac{E_{\text{line}}}{E_\gamma} \right) + \frac{\Theta}{m} \right] \times \\ \exp \left[ -\left( \frac{m}{2\Theta} \right) \left( \frac{E_\gamma}{E_{\text{line}}} + \frac{E_{\text{line}}}{E_\gamma} \right) \right] \end{aligned} \quad (77)$$

This equation can be recast in terms of  $\chi$  by using equations (10) and (12).

### 5.2.5. The effective absorption $N\sigma$

The absorption coefficient depends upon  $N$ , the number density of the clouds, and on  $\sigma$ , the absorption cross-section per cloud. These are in general a function of position. Since the pressure gradient and the inflow velocity in the  $\hat{r}$  and  $\hat{\theta}$  directions are ignored in our approximation of the flow, the density profile cannot be determined in a fully self-consistent manner via the mass continuity equation. To overcome this, we assume a simple two-parameter profile

$$N\sigma = \sigma_0 r^{-\beta}. \quad (78)$$

Where  $\sigma_0$  can be considered as a proportionality constant fixing the density and opacity scales. Without losing generality, we adopt a value  $\beta = 3/2$ . The results can then easily be generalized to other values of  $\beta$ . For the case of a swarm of absorbing clouds around a black hole, the optical depth is approximately one. This corresponds to the case where  $\sigma_0$  is of order 0.5 or greater, with the integration proceeding radially to the event horizon. The effective optical depth depends greatly on the paths the photons take.

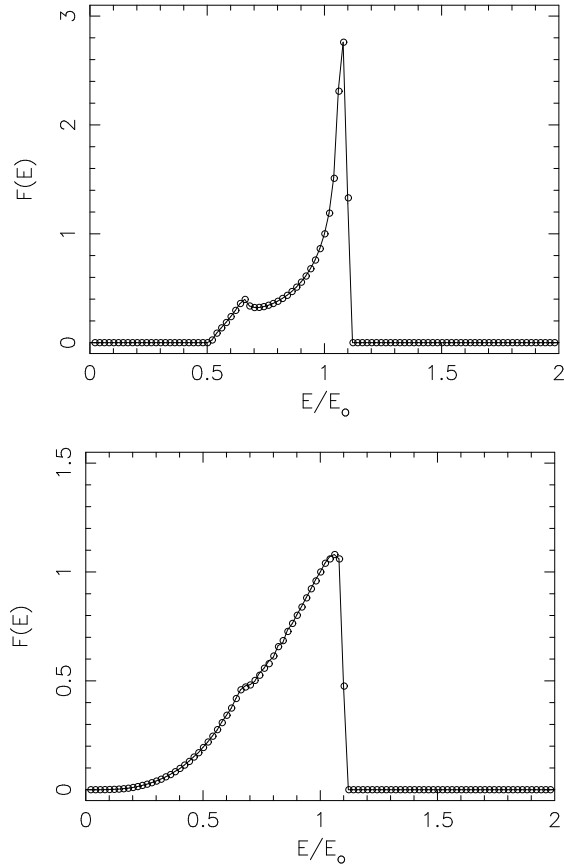


**Fig. 3.** The profiles of emission lines from thin Keplerian accretion disks around a Schwarzschild black hole (top) and a Kerr black hole with  $a = 0.998$  (bottom). The line profiles are normalized such that the flux  $F(E) = 1$  at  $E/E_0 = 1$ . The viewing inclination angle is  $45^\circ$ . The inner radius of the accretion disk is at the last stable orbit, and the outer radius is  $10R_g$ . The line emissivity on the disk surface is a power-law which decreases radially outward, and the powerlaw index is  $-3$ . Only emission contributed by the direct disk image is considered; emission from higher-order images is not included. The emission is unabsorbed. In each case, the solid lines correspond to the line profiles obtained by semi-analytic calculations described in Fanton et al. (1997), and the circles represent the line profile obtained by our numerical ray-tracing calculations.

## 6. Spectral Calculations

### 6.1. No absorption

#### 6.1.1. Accretion disks

We calculate the observed energy of the flux from a point on the planar disk using equation (12). We ignore absorption. The line emissivity has a power law profile, which decreases radially from disk centre. The intensity is proportional to the third power of the relative shift; the flux has an extra factor of  $\nu_0/\nu$  due to time dilation, i.e. it is proportional to the fourth power of the relative frequency

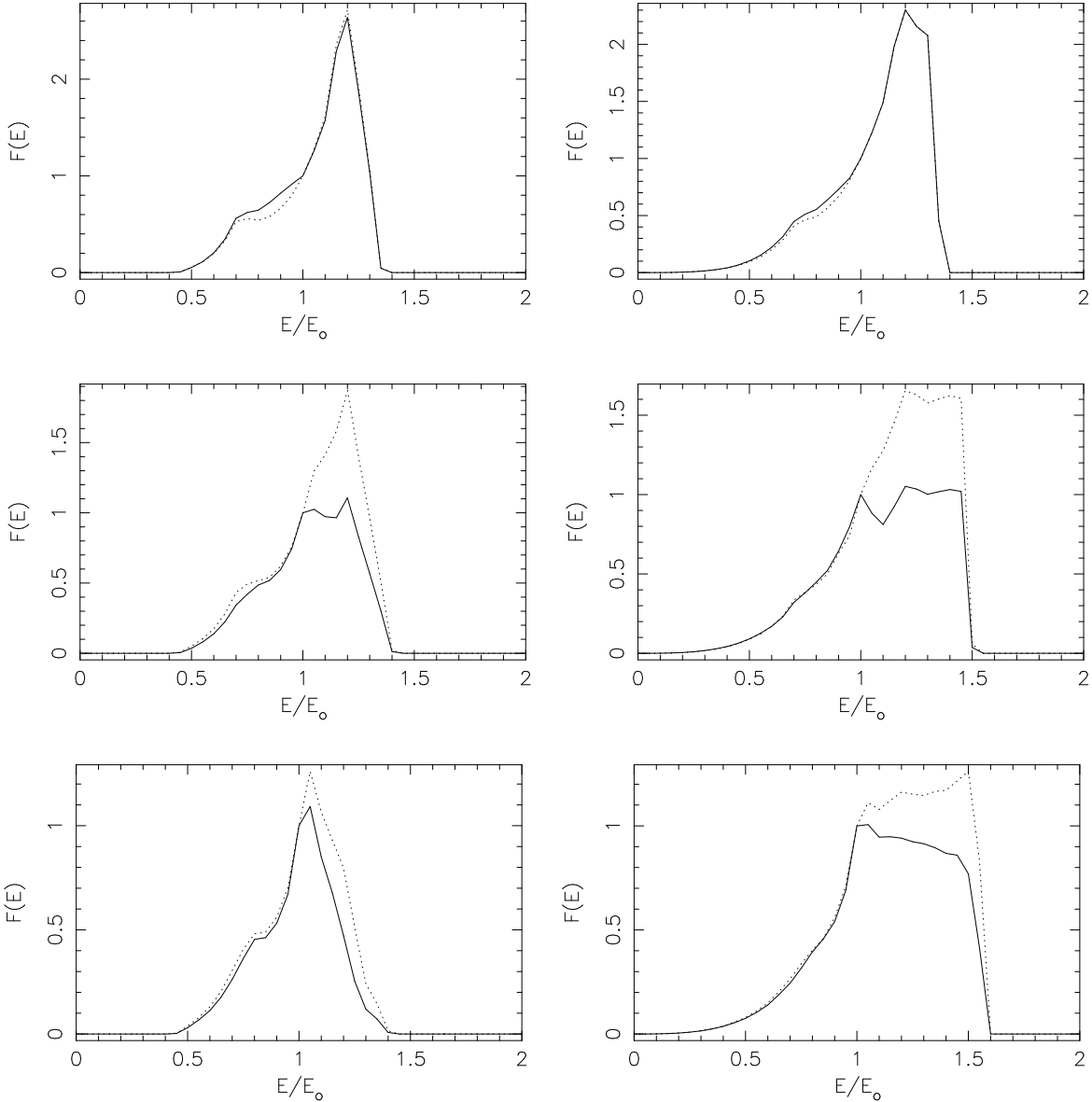


**Fig. 4.** Comparison of the line profiles for cases considering only the direct disk image (dotted line) and cases including high-order images (solid line). The line profiles are normalized such that  $F(E) = 1$  at  $E/E_0 = 1$ . The viewing inclination angles of the disks are  $75^\circ$ ,  $85^\circ$  and  $89^\circ$  (panels from top to bottom). Line profiles for Schwarzschild black holes are shown in the left column; line profiles for the Kerr black holes with  $a = 0.998$  are shown in the right column. The outer radius of the accretion disk is  $20R_g$ , and the index of the emissivity powerlaw is  $-2$ .

shift. (Note that  $F$  in §2 is the distribution function, not the flux of the emission.)

Our calculation reproduces the line profiles of direct images of accretion disks as those shown in Fabian et al (1989), Kojima (1991), Fanton et al (1997), Bromley et al (1997), and Reynolds et al (1999). Figure 3 shows two example line spectra calculated using the method described above. The spectra contain only emission from the direct image. We also show line spectra obtained using the method by Fanton et al (1997) for comparison. The results in the two calculations are in excellent agreement.

We also carry out spectral line calculations which include contribution from higher-order disk images. (Here and hereafter we assume that the emissivity powerlaw has an index of  $-2$ , except where otherwise stated explicitly, i.e.  $\mathcal{I}(\lambda_0) \propto r^{-2}$ ) Our calculations show that the contribution of the higher-order images are significant only at high inclination angles (see Fig. 4). The emission from high-order images is mostly at frequencies close to the rest frequency of the line, because the region where highly red and blue-shifted emission originates is obscured.

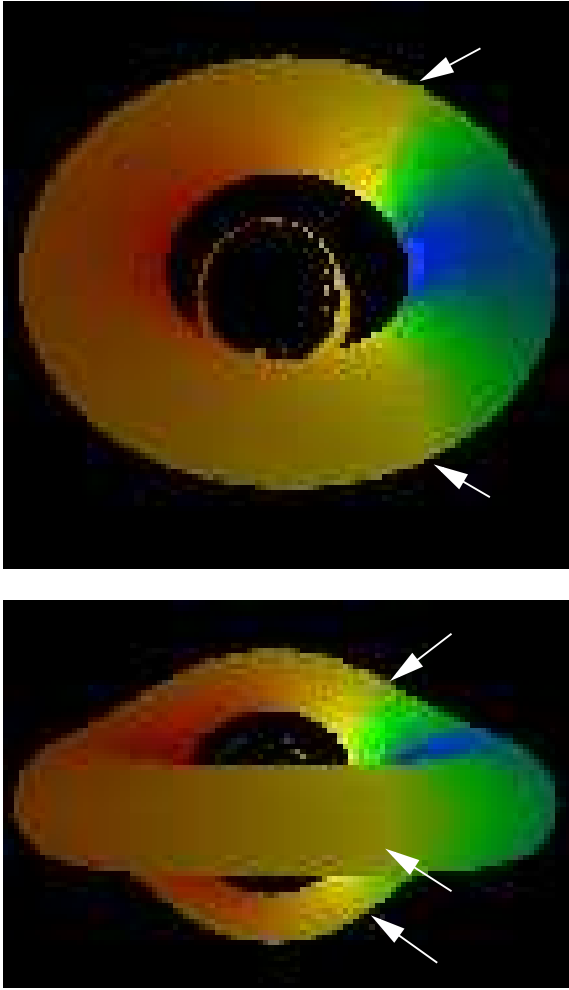


**Fig. 5.** Images of an accretion torus around a Kerr black hole viewed at inclination angles of  $45^\circ$  (top) and  $85^\circ$  (bottom). The angular momentum of the black hole  $a = 0.998$ . The torus is constructed using the velocity law in §4.2. The inner and outer radii are determined by the critical surface as described in the same section. High-order images are shown. The energy shift of the emission is represented by a false-colour map laid on the torus surface. Red-shifted emission is coloured yellow/red and blue-shifted emission is coloured blue. The grey lines indicated by the arrows mark the region where the emission has zero energy shift, separating the torus into regions with red and blue shifted emission.

#### 6.1.2. Rotational Torus

We now investigate the emission from an accretion torus. We consider a model in which the inner radius of the torus is determined by the marginally stable orbits of the particles. These marginally stable orbits, which depend on  $\omega$  and  $d\omega/dr$ , form a surface in a three-dimensional space. The marginally stable orbit for particles in Keplerian motion in the equatorial plane is  $6 R_g$  around a Schwarzschild black hole and is  $1.23 R_g$  around a Kerr black hole with  $a = 0.998$ . In equation (54), Keplerian motion corresponds

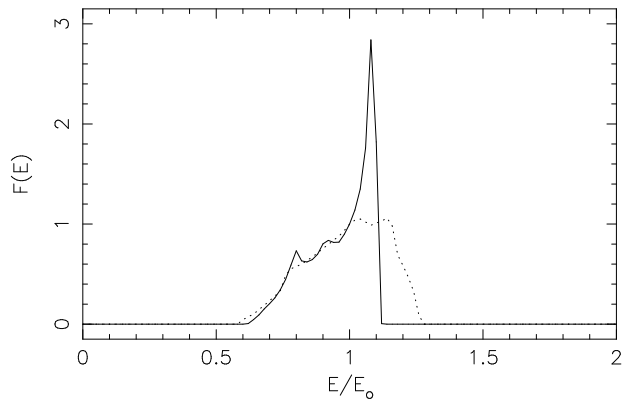


**Fig. 6.** Profiles of emission lines from an accretion torus around a Kerr black hole with  $a = 0.998$  at viewing inclination angles of  $45^\circ$  (solid line) and  $85^\circ$  (dotted line). The parameters of the torus are  $n = 0.21$  and  $r_k = 12R_g$  in the velocity profile equation (54).

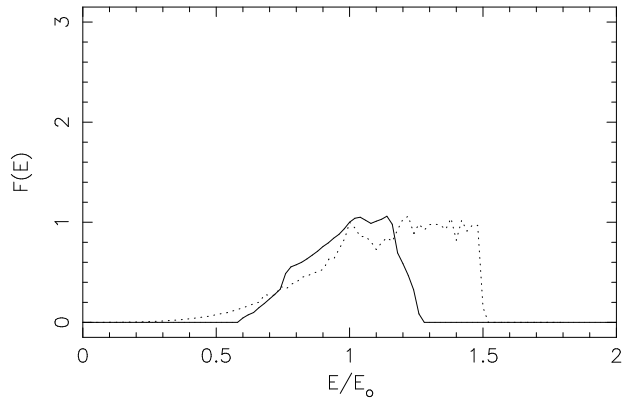


**Fig. 7.** A comparison of the profiles of lines from an accretion disk (dotted line) and an accretion torus (solid line) around a Kerr black hole with  $a = 0.998$ . The disk and the torus are viewed at an inclination angle of  $85^\circ$ . The parameters of the torus are the same as those in Fig. 6. The disk has an outer radius of  $20R_g$ , an inner radius of  $1.23R_g$ , and a Keplerian velocity profile.

to the case with the index  $n = 0$ . In the torus model that we consider here,  $n$  is not necessarily zero. As a consequence, the location of the marginally stable orbit of particles in the tori and conventional Keplerian disks are different. (See Fig. 1. in §4.2). We use a surface-finding algorithm to determine the boundary of the torus (see Appendix C).

In Fig. 5, we show three-dimensional images of the model torus around a Kerr black hole. We include the first four image orders. The inclusion of high order images is mandatory due to the ‘mixing’ caused by the extension out of the equatorial plane (Viergutz 1993). The torus is viewing inclination angles of  $45^\circ$  and  $85^\circ$  (top and bottom panels respectively). The left-right asymmetry is

caused by inertial-frame dragging. The multiple images are consequences of gravitational lensing. At small inclination angles, only the surface above the equatorial plane of the torus is seen in the direct image. At very large inclination angles, the surface below the equatorial plane is severely lensed and also becomes visible.

The false-colour map laid on the torus surface show the energy shift of the emitted photons (determined by equation [12]), as viewed by a distant observer. The separatrix, which corresponds to zero energy shift, divides the torus surface into regions of blue energy shift and regions of red energy shift. At large inclination angles the inner surface of the near side of the torus is not visible, and the inner surface of the far side is obscured by the near side of the torus. Thus, emission with the largest energy shifts is hidden. This is very different to the situation for a planar accretion disk – regardless of the viewing inclination and the visual distortion, the emission from the innermost part of the disk is always visible.

Figure 6. shows the resulting line profiles obtained by integrating the emission over the images shown in Fig. 5. The line profile of a torus viewed at  $45^\circ$  is similar to that of the planar accretion disk. It has a sharp blue peak and smaller red peak. It also has an extended red wing. This is due to the fact that the projections of a torus and a disk on the sky plane are very similar at low inclination angles.

However, our calculations show that geometric effects are very important for large viewing inclination angles. When some part of the emission region is self-obsured, the resulting profile, as observed from infinity, to be completely different from that of the flat disk (see Fig. 7.). For a torus with large viewing inclination angles, the inner surface of the torus tends to be obscured. This corresponds to the region where the most redshifted flux of the line is emitted (due to large transverse red shift and gravitational red shift). This makes the red wing less prominent. The outer surface of the torus is visible from all inclinations. As a result the line profile tends to be singly peaked, with the maximum at the unshifted line frequency due to the emission from the outer surface dominating. By altering the geometry of the emitter a wide variety of emission profiles can be obtained.

## 6.2. Resonant Scattering

We use a disk model to illustrate the resonant scattering effects. We assume the inner edge of the accretion disk is given by the marginally stable orbit. We use an outer disk radius of  $20R_g$  in all the disk simulations. This was chosen to accentuate the relativistic effects. The emission line profile is assumed to be a delta function. We collate the light from the first four image orders of the accretion disk.

The line profiles are obtained from  $750 \times 750$  pixel images. The intensity scale on the graphs is in arbitrary units. (It is just the log of the sum of pixel intensity over the image, as a function of frequency.) The x-axis of the

graph is in units of the line rest energy, with  $E/E_0 = 1$  corresponding to the unshifted line.

We bin the injection spectrum and the absorption coefficient linearly with energy. There are 1000 bins from  $E = 0$  to  $E = 2E_0$ . Since the thermal width of the line is small, we assume that the emission line is narrow, with a width of only one energy bin. After the calculation, we smooth over sets of ten adjacent bins to remove numerical noise which has a large scatter. See Appendix B for more information about the algorithm used.

We investigated two space-time models. One with  $a = 0$  corresponding to a Schwarzschild black hole, and one with  $a = 0.998$ , corresponding to a maximally spinning Kerr black hole. We have plotted spectra containing the continuum and the continuum plus line as we have varied the opacity of the absorbing clouds.

We have also shown how the spectra change with inclination due to geometric effects. We have included a nearly edge-on model ( $i = 85^\circ$ ), and a model with a moderate inclination of  $45^\circ$ . See Fig. 8. for the results of absorbing the power law continuum, and Fig. 9. for the results of absorbing both the line and continuum.

## 7. Discussion

We have modelled line profiles from accretion disks to demonstrate the use of a general formulation for transfer of radiation through relativistic media in arbitrary space-times. In this paper, we used the transfer of emission from AGN as an illustration. In this model, we parametrized the disk/torus to describe the emitters and the space-density distribution of the absorbers. We took into account relativistic effects on the bulk dynamics and the microscopic kinematic properties of the absorbing medium.

Resonant absorption/scattering of line emission from accreting black holes in the general relativistic framework had been investigated previously by Ruszkowski & Fabian (2000). In their study, a thin Keplerian disk was assumed and the absorbing medium is a spherical corona of constant density centred on the black hole. The corona is rotating, with local rates obtained by linear interpolation from the rotation rate of a planar Keplerian accretion disk and the rotation rate at the polar region caused by frame dragging due to the Kerr black hole. The Sobolov approximation was used in the resonant absorption calculations, and a Monte Carlo method determined the re-emission/scattering.

Our calculation is different to that of Ruszkowski & Fabian (2000) in the following ways. Firstly, the emitters are not confined to the equatorial plane, i.e. they can be thin accretion disks or thick tori. Secondly, the absorbing medium is a collection of (cold) clouds with relativistic motions. The number density distribution of the clouds is parametrized by a powerlaw decreasing radially. The local bulk (rotational) velocity of the clouds is determined by general relativistic dynamics, and the velocity dispersion is calculated from the Virial theorem. Thirdly, we do not assume the Sobolov approximation. The resonant condi-

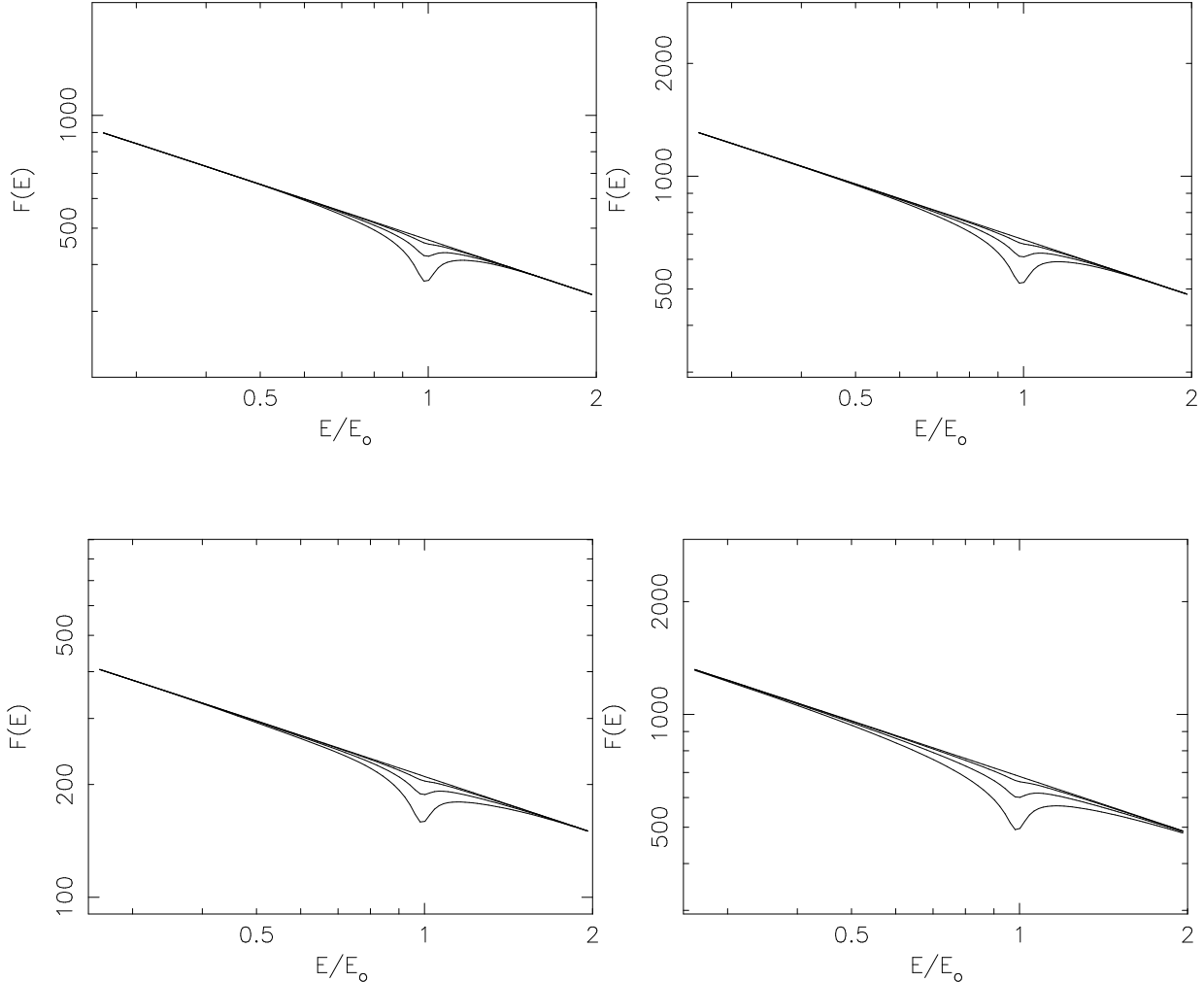


**Fig. 8.** Absorbed continuum emission from accretion disks around Schwarzschild and Kerr black holes with  $a = 0.998$  (left and right columns respectively), for  $i = 45^\circ$  and  $85^\circ$  (top and bottom panels respectively),  $\sigma_0 = 0, 0.05, 0.2$  and  $0.5$  (curves from top to bottom in each panel).

tion for the absorption coefficient is derived directly from the kinematics of the absorbing cloud particles. Fourthly, we ignore the contribution from re-emission to the line flux. However, we include emission from higher order disk images, in addition to the direct image.

One of the main differences between the two studies is the treatment of resonant absorption. In the Sobolov approximation, the absorption takes place locally (see Rybicki and Lightman 1979). The line profile is practically a delta function; otherwise, the assumption of quasi-local absorption breaks down. Moreover, it requires that the absorbing medium is a radial flow. The emission lines are broadened because of relativistic effects, and the motion of the medium is rotationally dominated. The locality of the absorption (required by the Sobolov approximation) therefore breaks down. To overcome these difficulties, we abandon the Sobolov approximation but, instead, employ full ray tracing.

In modelling the bulk flow, we derived the equation of motion of the absorbers using the rotational-support approximation for the accretion disk. In addition, we assume that the flow is supported out of the equatorial plane. There is negligible radial force in the equations of motion, and the radial velocity can be neglected. To include outflowing as a wind, or inflowing, requires additional components in the equation of motion. This complicates the formulation, in particular, when matching the flow boundary condition at the surfaces of the accretion disk/torus. A self-consistent boundary condition requires a dissipation mechanism in the boundary regions of the disk/torus and absorbing clouds. The inclusion of such dissipation is beyond the scope of this paper and this issue will be addressed in future works.

As the rays propagate from the accretion disk to the observer, they experience position-dependent absorption. The absorption depends upon the velocity profile of the

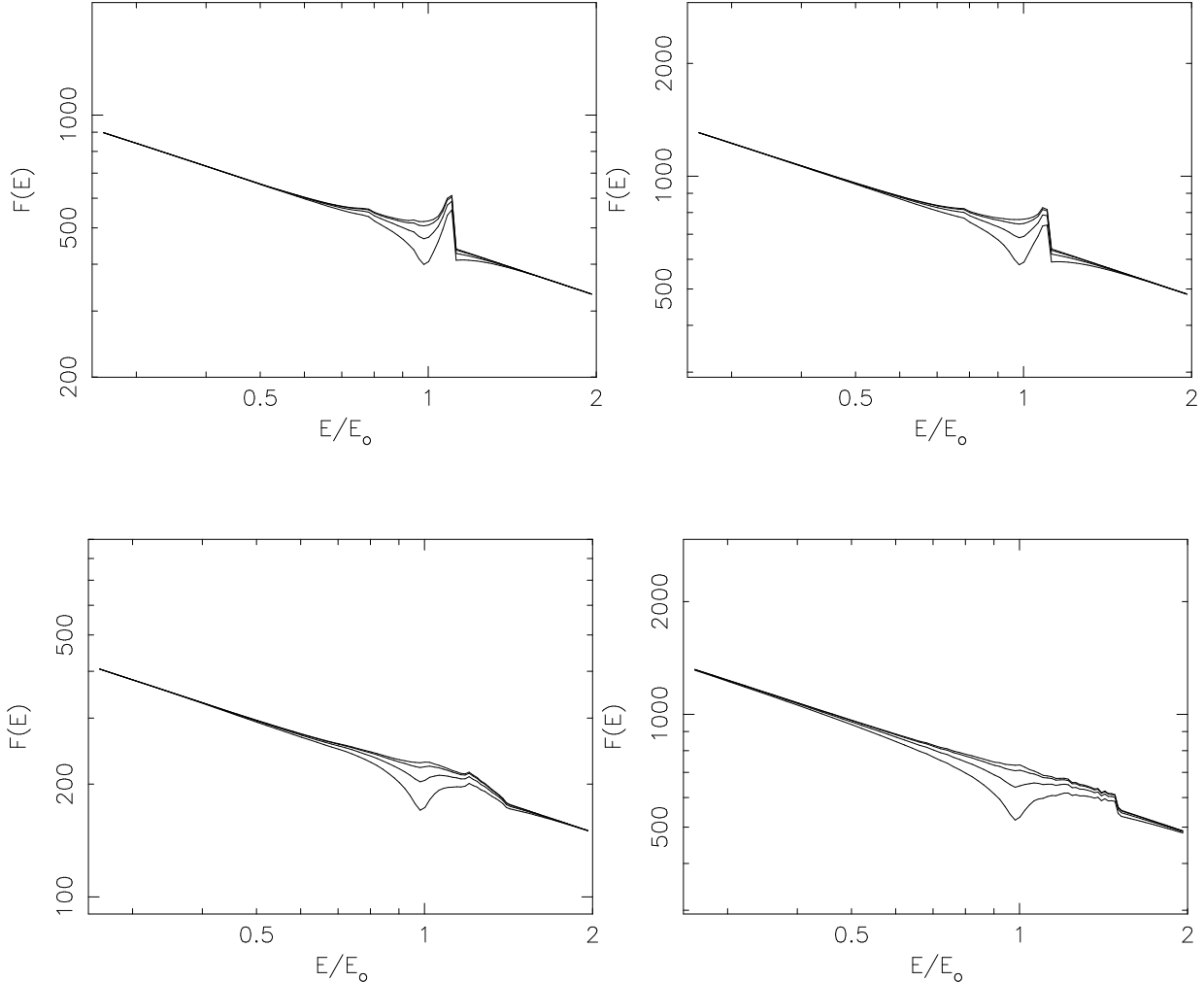


**Fig. 9.** Line and continuum emission from accretion disks around Schwarzschild and Kerr black holes with  $a = 0.998$  (left and right columns respectively), for  $i = 45^\circ$  and  $85^\circ$  (top and bottom panels respectively),  $\sigma_0 = 0, 0.05, 0.2$  and  $0.5$  (curves from top to bottom in each panel).

material as well as its density and the line profile function of the absorption coefficient. Since the absorbers are moving in relativistic speeds, the bulk velocity is an important factor. Lorentz contraction increases the absorption coefficient accordingly, and Doppler shift alters the frequency of the emission as seen by the absorbers.

The potential energy liberated by material infalling into a black hole is of order a few percent of the material's rest mass, and the energy corresponding to 'thermal' kinematic velocity dispersion approaches this rest mass energy. Thus, we replace the conventional Maxwellian distribution by the Jüttner distribution for relativistic particles in deriving the resonant line absorption coefficient. This distribution does not give a Gaussian absorption profile even in the bulk rest frame of the absorbers.

The absorption line profiles of the direct images show a dip around the line rest frequency (energy) ( $E/E_0 = 1$ ). Absorption can change the line profile significantly. The

flux around the rest frequencies is, however, augmented by the flux from shifted lines from the higher order images, especially at high disk inclination. These two effects compete, and when the line-of-sight optical depth is high, the contribution of the high-order images is masked.

## 8. Conclusion

We present a numerical ray-tracing method for radiative-transfer calculations in curved space time and apply the method to calculate line emission from accretion disks and tori around black holes. Our calculations have shown that lines from relativistic accretion tori have profiles very different to lines from relativistic thin planar accretion disks for the same system parameters, such as the spin of the black hole and the viewing inclination. The self-obscurcation of the inner region of the accretion torus leads to weaker red wing in the emission lines when compared

with the lines emitted from a thin planar accretion disk. At high inclination angles the strong blue peak is also absent in the line emission from the tori.

We also investigate the effects of resonant absorption/scattering by the line-of-sight material in relativistic motion with respect to the emitters in the disk/torus, and the observer. Our method does not invoke the Sobolov approximation, and the resonant absorption/scattering condition is derived directly. We have shown that absorption effects are important in shaping the profiles of emission lines. The interpretation of observations of relativistic lines from AGN is non-trivial when absorption is present.

*Acknowledgements.* We thank Mat Page for discussion, and Alex Blustin for comments on the manuscript. SVF acknowledges the support by a UK government Overseas Research Students Award and a UCL Graduate School Scholarship. We thank the referee for clarifying the issue regarding energy redistribution in the scattering process.

## References

Bao, G. 1992, *A&A*, 257, 594

Bao, G., Hadrava, P., & Ostgaard, E. 1994, *ApJ*, 435, 55

Bardeen, J. M., Press, W. H., & Teukolsky, S. 1972, *ApJ*, 178, 347

Baschek, B., Efimov, G. V., Waldenfels, W. von, & Wehrse, R. 1997, *A&A*, 317, 630

Bromley, B. C., Chen, K., & Miller, W. A. 1997, *ApJ*, 475, 57

Cadez, A., Fanton, C., & Calvani, M. 1998, *New Astronomy*, 3, 647

Cadez, A., Brajnik, M., Comboc, A., Calvani, M., & Fanton, C. 2003, *A&A*, 403, 29

Carter, B. 1968, *Phys. Rev.*, 174, 1559

Cunningham, C. T. 1975, *ApJ*, 202, 788

Cunningham, C. T. 1976, *ApJ*, 208, 534

Dabrowski, Y., Fabian, A. C., Iwasawa, K., Lasenby, A. N., & Reynolds, C. S. 1997, *MNRAS*, 288, L11

Fabian, A. C., Rees, M. J., Stella, L., & White, N. E. 1989, *MNRAS*, 238, 729

Fabian, A. C., Iwasawa, K., Reynolds, C. S., & Young, A. J. 2000, *PASP*, 112, 1145

Fanton, C., Calvani, M., De Felice, F., & Cadez, A. 1997, *PASJ*, 49, 159

Gerbal, D., & Pelat, D. 1981, *A&A*, 95, 18

Hawley, J. F., & Balbus, S. A. 2002, *ApJ*, 573, 738

Kojima, Y. 1986, *Prog. Theor. Phys.*, 75, 1464

Kojima, Y. 1991, *MNRAS*, 250, 629

Laor, A. 1991, *ApJ*, 376, 90

Lindquist, R. 1966, *Annals of Physics*, 37, 487

Matt, G., Perola, G. C., & Stella, L. 1993, *A&A*, 267, 643

Mihalas, D. 1980, *ApJ*, 237, 574

Misner, C. W., Thorne, K. S., & Wheeler, J. A. 1970, *Gravitation*, W. H. Freeman, San Francisco

Nobili, L., Turolla, R., & Zampieri, L. 1991, *ApJ*, 383, 250

Pariev, V. I., & Bromley, B. C., 1998, *ApJ*, 508, 590

Park, M., 1990, *ApJ*, 354, 64

Press, W. H., Teukolsky, S. A., Vetterling, W. T., & Flannery, B. P. 1992, *Numerical Recipes in Fortran*, 2nd Ed., Cambridge University Press, Cambridge

Reynolds, C. S., Young, A. J., Begelman, M. C., & Fabian, A. C., 1999, *ApJ*, 514, 164

Ruszkowski, M., & Fabian, A. C. 2000, *MNRAS*, 315, 223

Rybicki, G. B., & Lightman, A. P. 1979, *Radiative Processes in Astrophysics*, Wiley, New York

Smak, J. 1969, *Acta Astronomica*, 19, 155

Stella, L. 1990, *Nature*, 344, 747

Tanaka, Y., et al. 1995, *Nature*, 375, 659

Viergutz, S. U. 1993, *A&A*, 272, 355

Zane, S., Turolla, R., Nobili, L., & Erna, M. 1996, *ApJ*, 466, 871

## Appendix A: Frequency Bins

Using an astrophysical model together with the metric, we can obtain an equation describing the flow of the medium through which the ray is propagating;  $u^\alpha(x^\alpha(\lambda))$ . The properties and distribution of the medium can be used to derive the absorption and emission terms  $\chi_0(x^\alpha(\lambda))$  and  $\eta_0(x^\alpha(\lambda))$ . These can then be used to calculate what is observed from infinity via equation (17). In practice this simple method is altered with a ray-tracing numerical algorithm. The radiative transfer equation is not time-symmetric, so if one follows rays back from the observer to the emitter the above formulation cannot be used. The emission frequency and intensity is not known until the emitter is reached along the path.

This problem can be solved using one of two approaches. The first is to collate the path from emitter to observer, and then to integrate along that path forward in time using equation (17). The second approach is to collate the optical depth for  $\mathcal{I}$  for a table of frequencies as one travels back in time. This optical depth can then be used to calculate the observed intensity,  $I$ , for each binned frequency. The results for each emission element along the path are simply summed.

Since, in general, the resulting frequencies are binned anyway to get a spectrum, we choose the second method. It requires less storage, and is a simple extension of the grey-absorber case where  $\chi_0$  and  $\eta_0$  are no longer functions of  $\nu$ . In our treatment, we sum over the observed frequencies rather than those in the rest frame, avoiding the need to transform the distribution of the frequencies along the path due to the gravitational redshift factor. The act of going from the emission frame to the observer's frame also affects the intensity  $I$ , so we use the invariant  $\mathcal{I}$  instead, only converting to specific intensity just before outputting the results.

Binning the optical depth with frequency along a path also allows us to model the radiative transport of the continuum as well as the lines, provided that one is in the limit where scattering is unimportant. (Stimulated emission can be modeled by using a negative absorption coefficient.) Depending on the relative intensities of the continuum and the line, absorption may cause the emission feature to be converted into an absorption feature.

We assume that the continuum is a power law, which we parametrize by a slope and intensity at the line rest frequency. We have assumed that the continuum is emitted with an intensity that scales with the line emissivity. This means that the equivalent width of the emission line

is constant across the disk. We set this to be 0.05 of the rest line frequency. (This value is roughly what is seen in AGN.) To simplify things further, we will fix the power law index of the continuum to be  $\gamma = 0.5$ , where  $\gamma$  is defined by

$$I = CE^{-\gamma}, \quad (\text{A.1})$$

in which  $I$  is the continuum intensity as a function of energy,  $E$ , and  $C$  is derived from the given equivalent width. This rather hard spectrum was chosen to emphasise the line.

The treatment assumes that the continuum is created in a relatively thin planar structure above the accretion disk. In effect, we treat the emission from the disk corona as part of the injection spectrum, together with the emission line, which we propagate through the absorbing material suspended much higher above.

## Appendix B: Ray Tracing Algorithm

A direct ray-tracing method is used instead of the conventional transfer-function method, as it is easier to incorporate the numerical radiative-transport calculations. The ray-tracing algorithm is as follows:

1. Integrate the equations governing the geodesics, and those describing the optical depth for each frequency, from the observer to the emitting surface;
2. At each crossing of the equatorial plane / torus surface, collate the position and the direction of the photon;
3. Construct the image, and determine the observed frequency/energy shift;
4. Integrate the emission over the images of each order to produce the line profiles.

We use a Runge-Kutta integrator to calculate the ray trajectories. The relative tolerance is set to  $10^{-11}$ , which prevents the ray tracer from missing the torus by taking steps which are too large. It also allows a simple Eulerian method to be used to integrate the optical depths. The absorption coefficient is a slowly varying function on the scale of the step size, which allows this optimisation.

The foot points of the null geodesics (photon trajectories) on the disk surface are calculated by a root-finding algorithm (see e.g. Press et al. 1992, p.343). The first four intersections of the null geodesics and the disk plane (corresponding to the direct and first three higher-order images), and the four-vectors of the photons emitted from there are recorded. The incorporation of an emissivity law is therefore straightforward, as it is defined in terms of the spatial coordinates on the disk plane. Since the trajectory of the photon is also saved at each crossing point, it is also possible to include the effects of limb darkening, and to model a semi-transparent disk.

Since the disk is imaged upon a sky plane, all gravitational lensing effects on the intensity of the light are implicitly included in the calculation of the image itself. If a region of the disk is magnified then it will cover more

area in the image, and thus will appear brighter than a non-magnified region. Inclination effects are also included implicitly. An inclined disk will cover less pixels than a face-on disk, where the number of pixels is roughly proportional to  $\cos i$ , where  $i$  is the inclination angle. (Light bending causes this Euclidean formula to be only an approximation.) Gravitational lensing does not alter the observed surface brightness of a point.

This implicit inclusion of changing areas of photon flux-tubes linking the observer to the emitter vastly simplifies the calculation of the observed flux. All that is required is to integrate over each pixel on the image, taking into account the redshift of the emission regions corresponding to the pixels. If one were integrating over the surface of the disk, instead of over the image, then the Jacobian of the transformation from the disk to the image plane coordinates would be required. This is numerically difficult to obtain, and would require a separate transformation for each image order.

The programs (written in Fortran) take a few hundred kilobytes of memory under Tru64 Unix on a OSF1 V5.1 1885 Alpha. One version outputs the intensity / frequency shift of the emission line for each ‘pixel’ in the sky plane. Another version collates the continuum as well as the line, and outputs a table of intensity versus energy integrated over the whole disk. Depending on load on the shared system, and on the image size requested, a typical run takes a few hours per image.

## Appendix C: Surface Finding Algorithm

We consider the following algorithm to determine the torus surface. We integrate equation (51) and tabulate the resulting points  $(r, \theta)$  along the path of the integration. Then we interpolate  $(r, \theta)$  and construct the torus surface, where the emission originates. We use spline interpolation between the surface points.

When ray tracing the photon paths, we determine the intersection of the trajectory and the torus surface. As the photon trajectory calculations may take large spatial steps, there is a possibility that the torus is not ‘detected’. To prevent this from happening, we consider the following procedure. We take note of the region where the photon is located during the trajectory calculation: either inside or outside the torus and either above or below the equatorial plane. Whenever the photon leaves one of the four regions, and enters another region, we use a boundary-searching algorithm to find the exact location where the transit occurs. If the trajectory hits the equatorial plane outside the torus, the integration will continue. If the trajectory hits the torus, then integration is terminated.

By taking smaller steps required by the boundary-finding algorithm, we can prevent the integrator from missing the torus entirely. This algorithm can be used for more complicated surfaces. It works well, because the integrator will only miss intersections when the trajectory is close to tangential to a surface. This happens close to the equatorial plane in the torus models. Adding in a fake

boundary there, and thus decreasing the step size, helps in preventing missed intersections.